Scattering Mechanism Analysis of Man-Made Targets via Polarimetric SAR Observation Simulation

Lamei Zhang, *Senior Member, IEEE*, Yifan Chen, Ning Wang, Bin Zou, *Senior Member, IEEE*, and Shuo Liu, *Student Member, IEEE*

***Abstract*—Scattering mechanism analysis of a man-made target is critical for polarimetric synthetic aperture radar (PolSAR) image feature extraction and image interpretation. The most straightforward method for scattering mechanism investigation of man-made target is to analyze a huge amount of measured data under various conditions. However, the acquirement of measured data is extremely expensive and time consuming, coupled with its poor reusability, which makes the investigation inefficient and costly. The electromagnetic (EM) simulation is an effective and convenient way to obtain PolSAR data by solving equations describing the EM scattering from target of interest. It is adaptable to any observation condition, targets or environments, which have become a powerful tool commonly used for the study of EM scattering mechanism of target. In this article, an efficient simulation framework for the emulation of PolSAR operation and imaging is proposed. This framework is based on ray tracing integrated with geometrical optics, physical optics, and Kirchhoff approximation. The simulated image of a family car is in good agreement with the measured data of MiniSAR platform. Besides, images of T-72 tank under various observation conditions, radar parameters and terrains are simulated. Freeman decomposition is employed and scattering component percentages of target under different conditions are presented to analyze the scattering mechanism in detail.**

***Index Terms*—Man-made targets, polarimetric synthetic aperture radar (PolSAR) image simulation, ray tracing, scattering mechanism.**

I. Introduction

POLARIMETRIC synthetic aperture radar (PolSAR) has garnered increasing attention in recent years as it provides more information of target than the SAR system with single polarimetric channel. Nowadays, with the improvement of resolution, PolSAR data has been more widely used for man-made target recognition and classification [1]–[5]. As a result, scattering mechanism analysis of target becomes very important because it provides comprehensive information about the structures of the target, which is very helpful for recognition and classification of targets. For better exploitation of PolSAR data, the analysis of scattering mechanism of target is well warranted.

The scattering characteristics of targets are strongly associated with background environments, orientation angles of target and radar parameters. The research of target scattering mechanism is to establish the relationship between target scattering characteristics on PolSAR data and these factors. In order to analyze the scattering mechanism, a tremendous amount of PolSAR data collected under diverse conditions is required. However, the acquisition of measured data is difficult and expensive. Therefore, PolSAR image simulation using electromagnetic (EM) scattering computation becomes an efficient way to generate data under various conditions.

Considerable research efforts have been devoted to develop SAR or PolSAR simulators. Using empirical model or point-scattering model is one of the simplest ways to generate SAR or PolSAR images [6]–[8]. The computation speed of these approaches is high but the accuracy is relatively low. For more precise simulation of raw signal, EM scattering computation methods are used to simulate the propagation and reflection of EM wave. Full-wave EM methods, such as finite-difference time-domain method, are common ways to perform EM scattering calculation. Nevertheless, this category of methods consumes a huge amount of computational time and memory, which may only suitable for simulation of small-sized targets [9]–[12]. High-frequency approximation methods are more appropriate to calculate the raw signal of SAR or PolSAR system, since they can be adapted to large and complex simulation scene [13], [14]. Some commonly used high-frequency approximation methods, such as geometrical optics (GO), physical optics (PO), small perturbation method, physical diffraction theory (PTD), are often used to calculate the scattered field of large scene [15]–[18]. Shooting bouncing ray method is another commonly used method to predict the radar cross section of target, which takes multiple scattering into consideration [19], [20]. The idea of ray tracing is quite suitable for EM simulation of complex structures with multiple reflection [21]–[23]. A considerable amount of research about EM scattering calculation has been conducted. However, less attention has been paid to PolSAR image simulation based on these methods.

Based on SAR or PolSAR simulator, much research has been devoted to scattering mechanism analysis of large man-made objects. In [24], a multipath intensity model is used to generate

Manuscript received August 26, 2021; revised October 25, 2021 and December 3, 2021; accepted December 29, 2021. Date of publication December 31, 2021; date of current version January 14, 2022. This work was supported in part by the Science Foundation of the National Key Laboratory of Science and Technology on Advanced Composites in Special Environments under Grant JCKYS2020603C007 and in part by the National Natural Science Foundation of China under Grant 61871158. *(Corresponding author: Bin Zou.)*

Lamei Zhang, Yifan Chen, Bin Zou, and Shuo Liu are with the Department of Information Engineering, Harbin Institute of Technology, Harbin 150001, China (e-mail: zzbei@hit.edu.cn; yifan_chen111@163.com; zoubin@hit.edu.cn; liushuo_1993@qq.com).

Ning Wang is with the Beijing Institute of Radio Measurement, Beijing 100000, China (e-mail: wangningtop@163.com).

Digital Object Identifier 10.1109/JSTARS.2021.3139668

bistatic SAR images of a ship-ocean scene and some features of images are analyzed. Ship rotation effects, including pitch, yaw and roll rotations, on SAR images are analyzed in [25] through a simulated dataset obtained by PO method. In [26], PO and PTD are used to simulate the PolSAR images of vessel and SDH decomposition is performed to analyze the scattering mechanism. A SAR simulator is used to study the ship scattering and a new feature vector is proposed for further target classification in [27].

Nevertheless, the scattering mechanism of small ground targets in PolSAR images attracts less attention. Generally, the polarimetric scattering mechanism of ground targets varies considerably under different radar parameters, observation conditions, background surface parameters, etc.

In order to acquire PolSAR data under different conditions quickly and analyze the scattering mechanism of man-made targets, an efficient simulation framework is presented to emulate the operation and imaging process of PolSAR in this article. Ray tracing based on GO, PO, and Kirchhoff approximation (KA) is used to simulate the raw signals and generate PolSAR images. The surface of target is meshed into triangular elements to perform ray tracing, which simulates the propagation of EM wave. On the basis of GO, PO, and KA, the polarimetric backscattering coefficients of each triangle mesh is calculated. In this case, raw signal of polarimetric SAR can be generated by multiplying the polarimetric backscattering coefficients with the emission signal in frequency domain. Based on the raw signal, range-Doppler (R-D) imaging algorithm is performed to obtain simulated polarimetric SAR images. In order to validate the proposed simulation method, the simulated image is compared with the measured MiniSAR image. In addition, a scenario including a T-72 tank is built for the analysis of scattering mechanism. The PolSAR data is simulated under various observation conditions, radar parameters and terrains. Freeman decomposition is employed and scattering component percentages are presented to analyze the scattering mechanism of the tank.

The rest of this article is organized as follows: In Section II, the principle of ray tracing integrated with GO/PO/KA hybrid method is given in details. Based on this, the process of PolSAR image simulation using the polarized backscattering coefficients is described. In Section III, the simulation PolSAR images of a cube with Freeman decomposition result are presented to prove the validity of ray tracing. Moreover, PolSAR images of a car are simulated under the same observation condition of MiniSAR system and compared with the measured data to illustrate the correctness of the proposed method. In Section III-D, several simulation experiments of the T-72 tank model are performed under different observation conditions, target parameters, and background parameters. Freeman decomposition is used to analyze the differences of the scattering mechanism under these conditions.

II. Polarimetric SAR Observation Simulation

A. Polarimetric SAR Simulation Framework

In this article, the framework of the polarimetric SAR simulation contains three main parts, ray tracing with GO/PO/KA, echo calculation and imaging, as shown in Fig. 1. Radar echo of arbitrary targets under various observation conditions can be acquired and the PolSAR images can be simulated by the proposed method. The detailed procedures are described as follows.

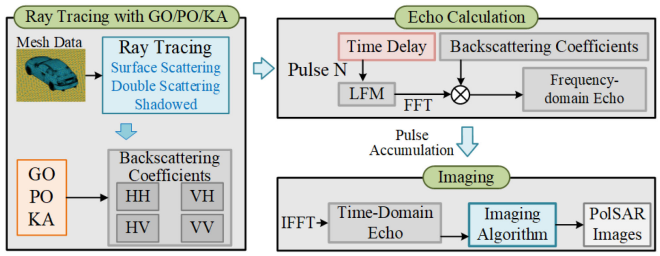

Fig. 1. Polarimetric SAR simulation framework.

1) *Ray Tracing With GO/PO/KA:* Ray tracing needs to be performed first to the triangular mesh data of the simulation scenario before EM scattering calculation. The scatterings of all the facets are classified into three categories: surface scattering; double bounce scattering; and shadowed. After ray tracing, GO, PO, and KA are performed to calculate the polarimetric backscattering coefficient of each mesh facet.
2) *Echo Calculation*: Assuming that linear frequency modulation (LFM) signal is emitted by radar, the polarimetric backscattering coefficients of each facet are multiplied with the LFM signal with time delay in frequency domain. Add the echo of each facet in different polarization channels together to obtain the frequency domain echo of the current pulse.
3) *Imaging*: Accumulate all the pulses of the whole scene and perform inverse fast Fourier transform (IFFT) to transform the echo signals into time domain. R-D imaging algorithm is applied to the echo signals of different polarization channels and the simulated polarimetric SAR images can be obtained.

B. Ray Tracing With GO/PO/KA Hybrid Method

The key to polarimetric SAR simulation is the accurate calculation of polarimetric backscattering coefficients. Although traditional full-wave computational EM techniques are of high accuracy, they cannot be applied to perform the polarized EM scattering calculation from large-scale scenario at high frequencies due to the enormous computation burden. In this situation, ray tracing with GO/PO/KA hybrid method is applied to perform the EM simulation in this article. The hybrid method can be applied to calculate the polarized radar echo of targets on an arbitrary rough surface. Based on this, the scattering mechanism of arbitrary target under the PolSAR system can be analyzed. We mainly focus on the man-made ground targets in this article. However, the proposed method can be applied to other natural ground targets, as long as those targets can be modeled by triangular mesh.

Based on the results of ray tracing, different methods are selected to perform EM scattering calculation on targets and background surface. GO is for reflection coefficient calculation

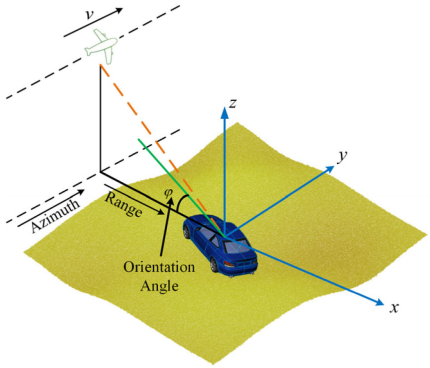

Fig. 2. Geometry of simulation scene.

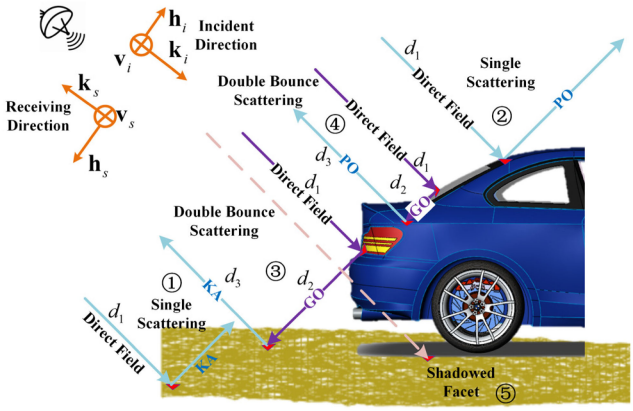

Fig. 3. Mechanism of ray tracing.

when multiple scattering occurs. KA is able to provide the scattered field of rough surface while PO is suitable for the scattered field calculation of smooth target. Both KA and PO are able to determine the backscattered field and polarimetric backscattering coefficients [28].

The geometry of the simulation is shown in Fig. 2. The polarimetric SAR platform moves along the y-axis at a speed of v and transmits radar signals along x-axis. The target is located at the center of coordinate system with an orientation angle of φ and the ground surface lies on the oxy plane. Generally, single-scale random rough surface cannot accurately simulate the real undulating ground. Hence, double-scale random surface is used to simulate the rough terrain surface, which is composed of two Gaussian random rough surfaces with different root mean square (RMS) heights and correlation lengths. Since the ground is uneven, the attitude of target needs to be adjusted according to the gradient of ground where the target locates.

As shown by Fig. 3, the composite scattering field from the target and its underlying rough surface is given by summing up four parts: the direct scattering from the rough surface (case ①) and target (case ②), the scattering contribution of the rough surface from the reflected wave of the target (case ③) and of the target from the reflected wave of the rough surface (case ④). Therefore, backscattering coefficients are calculated by different methods under different cases as well. For case ①, the backscattering coefficient will be directly calculated by KA since KA provides the approximate analytical solution to the rough-surface scattering [29]. For case ②, PO is used to calculate the backscattering coefficient. For cases ③ and ④, GO is used to calculate the reflection coefficient of the first reflection. If the EM wave is reflected to the ground, KA is used to calculate the backscattering coefficient of the second reflection. Otherwise, PO is used if the wave is reflected to the target. According to the theorem of KA and PO, the induced currents on the shadowed facets are zero and thus the scattering fields of them will not be calculated. Therefore, the backscattering coefficient is zero in case ⑤.

Supposing that all the models satisfy the validity condition of GO, PO, and KA, the backscattering coefficient calculation of each facet can be summarized as

$$\sigma_m(\hat{\mathbf{p}},\hat{\mathbf{q}},k)=\begin{cases}\sigma_{KA-m}(\hat{\mathbf{p}},\hat{\mathbf{q}},k) & \text{case ①}\\ \sigma_{PO-m}(\hat{\mathbf{p}},\hat{\mathbf{q}},k) & \text{case ②}\\ \Phi_{GO-m'}(\hat{\mathbf{p}})\sigma_{KA-m}(\hat{\mathbf{p}},\hat{\mathbf{q}},k) & \text{case ③}\\ \Phi_{GO-m'}(\hat{\mathbf{p}})\sigma_{PO-m}(\hat{\mathbf{p}},\hat{\mathbf{q}},k) & \text{case ④}\\ 0 & \text{case ⑤}\end{cases} \tag{1}$$

where $\hat{\mathbf{p}},\hat{\mathbf{q}}\in\{\mathbf{h}_i,\mathbf{v}_i\}$ is the polarization vector of incident and scattered wave, $\mathbf{h}_i$ and $\mathbf{v}_i$ represent horizontal and vertical polarization vectors of EM wave, $k=2\pi/\lambda$ is the wave number and λ is the wavelength.

The KA solution can be derived from the scattering field solution of integral equation method [30], expressed as

$$\mathbf{E}^{(s)}(\mathbf{r})=-\frac{ik\exp(-ikr)}{4\pi r}\left(I-\hat{\mathbf{k}}_s\hat{\mathbf{k}}_s\right)\cdot\int_S\left\{\hat{\mathbf{k}}_s\times[\hat{\mathbf{n}}\times\mathbf{E}(\mathbf{r}')]+\zeta_1[\hat{\mathbf{n}}\times\mathbf{H}(\mathbf{r}')]\right\}\exp(i\mathbf{k}_s\cdot\mathbf{r}')\,dS' \tag{2}$$

where r is the slant range, $\hat{\mathbf{k}}_s$ is the unit vector of observation direction, $\hat{\mathbf{n}}$ is the unit normal vector of the facet, $\mathbf{r}$ is the vector of observation point, ζ_1 is the intrinsic impedance, $\mathbf{E}(\mathbf{r}')$ and $\mathbf{H}(\mathbf{r}')$ are the EM fields at the position of facet.

According to the KA solution, the backscattering coefficient of facet m can be written as

$$\sigma_{KA-m}(\hat{\mathbf{p}},\hat{\mathbf{q}},k)=\hat{\mathbf{q}}\cdot\left(I-\hat{\mathbf{k}}_s\hat{\mathbf{k}}_s\right)\cdot\mathbf{F}_p(\alpha,\beta)\cdot\iint\exp[-i(\mathbf{k}_i-\mathbf{k}_s)\cdot\mathbf{r}']\,dm \tag{3}$$

$$\begin{aligned}\mathbf{F}_p(\alpha,\beta)=&\left\{\left(\hat{\mathbf{p}}\cdot\hat{\mathbf{h}}_l\right)\left[\hat{\mathbf{k}}_s\times\left(\hat{\mathbf{n}}\times\hat{\mathbf{h}}_l\right)\right](1+R_h)\right.\\&+(\hat{\mathbf{p}}\cdot\hat{\mathbf{v}}_l)\left[\hat{\mathbf{k}}_s\times(\hat{\mathbf{n}}\times\hat{\mathbf{v}}_l)\right](1+R_v)\\&+\left[(\hat{\mathbf{p}}\cdot\hat{\mathbf{v}}_l)\left(\hat{\mathbf{n}}\times\hat{\mathbf{h}}_l\right)(1-R_v)\right.\\&\left.\left.-\left(\hat{\mathbf{p}}\cdot\hat{\mathbf{h}}_l\right)(\hat{\mathbf{n}}\times\hat{\mathbf{v}}_l)(1-R_h)\right]\right\}\\&\times\sqrt{1+\alpha^2+\beta^2}\end{aligned} \tag{4}$$

where $\hat{\mathbf{v}}_l=\frac{\hat{\mathbf{n}}\times\hat{\mathbf{k}}_i}{|\hat{\mathbf{n}}\times\hat{\mathbf{k}}_i|}$, $\hat{\mathbf{h}}_l=\hat{\mathbf{k}}_i\times\hat{\mathbf{v}}_l$, $\mathbf{k}_i=k\hat{\mathbf{k}}_i$, $\mathbf{k}_s=k\hat{\mathbf{k}}_s$, $\hat{\mathbf{k}}_i$ is the unit vector of propagation direction, R_h,R_v are the Fresnel reflection coefficients for horizontal polarization and vertical polarization, α,β are the angles between $\hat{\mathbf{n}}$ and x-axis and y-axis respectively. Gordon integral algorithm [31] is applied to calculate the integral of (3).

PO is applied to calculate the backscattering coefficient of a facet on the target, which can be expressed as

$$\sigma_{PO-m}\left(\hat{\mathbf{p}},\hat{\mathbf{q}},k\right)=\hat{\mathbf{q}}\cdot\left[\hat{\mathbf{k}}_s\times\left(\hat{\mathbf{n}}\times\mathbf{G}\left(\hat{\mathbf{p}}\right)\right)\right]\times\hat{\mathbf{k}}_s\cdot\iint\exp\left[-i\left(\mathbf{k}_i-\mathbf{k}_s\right)\cdot\mathbf{r}'\right]dm \quad (5)$$

where $\mathbf{G}(\hat{\mathbf{p}})=(\hat{\mathbf{p}}\cdot\hat{\mathbf{h}}_l)\cdot\hat{\mathbf{v}}_l-(\hat{\mathbf{p}}\cdot\hat{\mathbf{v}}_l)\cdot\hat{\mathbf{h}}_l$.

Assuming that a dihedral corner reflector is formed between m and another facet m', the backscattering coefficient of m will be obtained by multiplying the reflection coefficient of m' calculated by GO and the backscattering coefficient of m calculated by KA or PO.

According to the GO theory, the reflection coefficients of one facet m' can be given by

$$\Phi_{GO-m'}\left(\hat{\mathbf{p}}\right)=\left[\begin{array}{cc}R_h & R_v\end{array}\right]\cdot\hat{\mathbf{p}}_{\hat{\theta},\hat{\phi}}\cdot\sqrt{\frac{dS_1}{dS_2}} \quad (6)$$

where $\hat{\mathbf{p}}_{\hat{\theta},\hat{\phi}}$ is the polarization vector of incident wave under spherical coordinate system, dS_1 and dS_2 are the cross-sectional areas of the ray tubes before and after reflection. Based on the results of ray tracing, if the EM wave is reflected onto the ground surface, KA is used to calculate the backscattering coefficient of m. Otherwise, PO is used for calculation.

In conclusion, combining (1), the backscattering coefficient of facet m is calculated only by KA or PO if no dihedral corner reflector is formed with it. When a dihedral corner reflector is formed between facets m and m', the backscattering coefficient of facet m is calculated by multiplying the reflection coefficient of m' and the backscattering coefficient of m. In this case, $\hat{\mathbf{k}}_i$ of m needs to be changed into the reflection vector of m'.

C. Polarimetric SAR Echo Calculation and Imaging

After computing the polarimetric backscattering coefficients of the target/surface model, the radar echo signals is computed. Assuming that LFM signal is emitted by radar, the echo signal of facet m can be written as

$$s_m\left(t,t_n\right)=a_r\left(t-\frac{R_m\left(t_n\right)}{c}\right)\exp\left[j\pi\mu\left(t-\frac{R_m\left(t_n\right)}{c}\right)^2\right]\times\exp\left[-j\frac{2\pi}{\lambda}R_m\left(t_n\right)\right] \quad (7)$$

where μ is the chirp rate, t_n is the time of pulse n, $a_r(\cdot)$ is a rectangular window function, and $R_m(t_n)$ is the propagation distance of the ray incident on facet m. Taking Fig. 3 as an example, the propagation distance is calculated by

$$R_m\left(t_n\right)=\begin{cases}2d_1 & \text{Surface scattering}\\ d_1+d_2+d_3 & \text{Double bounce scattering.}\\ 0 & \text{Shadowed}\end{cases} \quad (8)$$

To perform the multiplication between time-domain signals and backscattering coefficients, signals need to be transformed to frequency domain. The frequency-domain echo signals of all facets are added up to obtain those of the whole scenario.

TABLE I
PARAMETERS OF THE POLARIMETRIC SAR SYSTEM

Parameters	Value	Parameters	Value
Center frequency	16.8GHz	Sampling frequency	2.16GHz
Pulse Repetition Frequency (PRF)	2880Hz	Pulse width	0.5 μs
Bandwidth	1.8GHz	Platform speed	100m/s
Height	2914m	Resolution	$0.1m\times0.1m$
Look angle	28°	Polarization	HH, HV, VH, VV

For pulse n, the frequency-domain echo signal can be written as

$$S_n\left(\hat{\mathbf{p}},\hat{\mathbf{q}},f\right)=\sum_{m=1}^{M}\left[\sigma_m\left(\hat{\mathbf{p}},\hat{\mathbf{q}},\frac{2\pi f}{c}\right)\cdot\mathrm{FFT}\left(s_m\left(t,t_n\right)\right)\right] \quad (9)$$

where M is the total number of facets, $f\in[f_c-\frac{B}{2},f_c+\frac{B}{2}]$, f_c is the center frequency, B is the bandwidth and FFT$(\cdot)$ represents fast Fourier transform. The backscattering coefficient of the facet m of pulse n is represented by $\sigma_m(\hat{\mathbf{p}},\hat{\mathbf{q}},\frac{2\pi f}{c})$.

The frequency-domain echo signals of each pulse are calculated and then IFFT is performed to them so that time-domain echo signals can be obtained. Eventually, a traditional R-D imaging algorithm is applied to the time-domain echo signals of different polarization channels to get the simulated polarimetric SAR images.

III. Scattering Mechanism Analysis and Discussion

A. Simulation System Parameters

In this section, the experiments are conducted to validate the proposed polarimetric SAR simulation method. The MiniSAR system is a high-resolution, single-polarized system and the detailed parameters are given in Table I. The radar parameters, such as the center frequency, bandwidth, look angle, and resolution of the simulation system, are set up according to those of MiniSAR system. However, in order to analyze the polarimetric scattering characteristics of the target, the simulation system is set as a fully polarimetric SAR system, namely the polarization modes include HH, HV, VH, and VV.

All the target models in our simulations are built by SolidWorks 2016, whose material is considered as perfect electric conductor. The relative permittivity and conductivity of the ground surface are 1.7 and 0.01 S/m, respectively, which are assigned to each mesh facet as material parameters. The EM properties of the ground are set up according to those of cement [32], [33].

B. Scattering Mechanism Validation of Smooth Cube

Above all, a model of a smooth cube and a random ground surface with fluctuation is given to prove the validity of ray tracing. The size of the cube is $3\ \mathrm{m}\times3\ \mathrm{m}\times2\ \mathrm{m}$ with orientation angle of 0° , which is shown in Fig. 4.

The ground surface is composed of two Gaussian random rough surfaces. The height of each location (x,y) on the surface

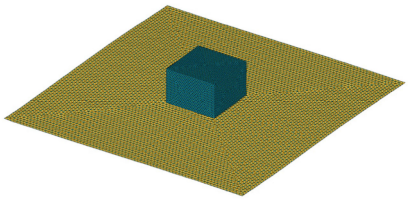

Fig. 4. Model of a cube and a random surface.

TABLE II
PARAMETERS OF THE GROUND SURFACE

Random surface	RMS height(cm)	Correlation length(cm)
Small-scale random surface	2	4.6
Large-scale random surface	0.5	500

can be written as

$$z(x,y) = z_1(x,y;l_1,\delta_1) + z_2(x,y;l_2,\delta_2) \tag{10}$$

where $l_1, \delta_1; l_2, \delta_2$ are the RMS heights and correlation lengths of small-scale and large-scale random rough surface, respectively. The height of each random surface can be calculated by

$$\begin{aligned} z(x,y;l,\delta) = \frac{2\pi}{L} \sum_{a=-A/2+1}^{A/2} \sum_{b=-B/2+1}^{B/2} & [S(k_a,k_b)]^{\frac{1}{2}} \\ & \cdot \exp(j(k_a x + k_b y)) \\ & \cdot \begin{cases} \frac{N(0,1)+jN(0,1)}{\sqrt{2}} & a \neq 0, \frac{A}{2} \text{ and } b \neq 0, \frac{B}{2} \\ N(0,1), & a = 0, \frac{A}{2} \text{ or } b = 0, \frac{B}{2} \end{cases} \end{aligned} \tag{11}$$

where L is the length of surface, A, B are the numbers of discrete points in the x and y directions, respectively, $N(0,1)$ is the standard normal distribution, $k_a = 2\pi a/L, k_b = 2\pi b/L$, $S(k_a, k_b)$ is the power spectral density function of rough surface, which can be written as

$$S(k_a,k_b) = \delta^2 \frac{l^2}{4\pi} \exp\left[-\frac{l^2}{2}\left(k_a^2 + k_b^2\right)\right]. \tag{12}$$

In this experiment, the size of the ground surface is $15\ \mathrm{m} \times 15\ \mathrm{m}$ and the detailed parameters of the random distribution are given in Table II.

The simulated polarimetric SAR images are shown in Fig. 5(a)–(c). The VH channel image is not included because it shows high similarity to the HV channel image. The simulated polarimetric SAR images show clear effects of shadow and layover. According to scattering theory of polarized wave [34], the scattering of a flat plane in cross-polarized channel is much weaker than that in co-polarized channel. Therefore, the scattering intensity of target in Fig. 5(b) is relatively weak. Moreover, speckle noise is quite obvious in the simulated images. This property is typical of the SAR/PolSAR images caused by the coherent superposition of reflected waves from many scattering elements [35]. In the process of simulation, the echo of each pulse is calculated. Therefore, the phenomenon of the speckle noise is formed naturally.

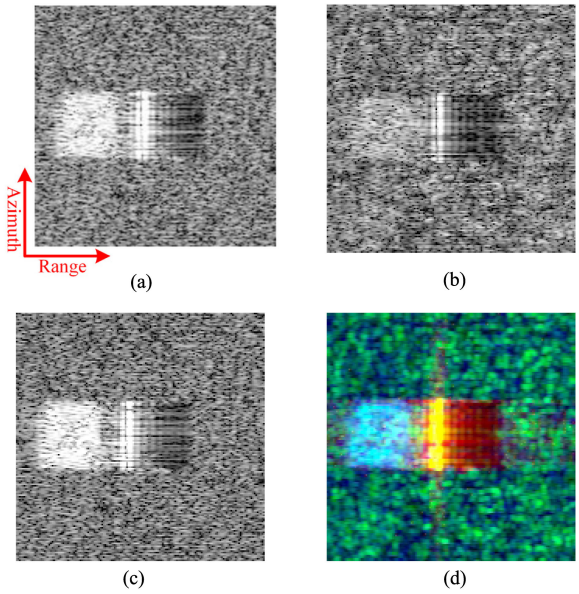

Fig. 5. Simulated polarimetric SAR images of a cube with Freeman decomposition result.

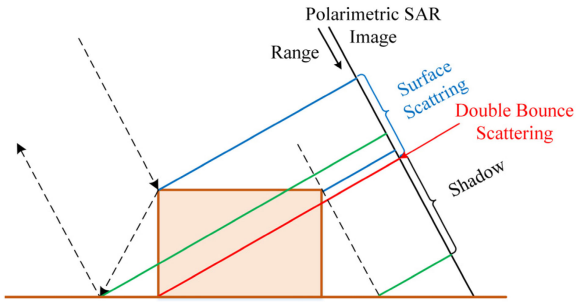

Fig. 6. Analysis of slant ranges.

In order to validate the simulated polarimetric scattering mechanism, Freeman decomposition [36] is used to decompose the simulated polarimetric SAR images. The Freeman decomposition is one of the most classic target decomposition methods for PolSAR image scattering mechanism decomposition, which is convincing and authoritative. Three types of scattering mechanism can be revealed, namely surface, double bounce, and volume scattering. The decomposition method is easy to implement and can be very helpful for the scattering mechanism analysis of our simulated results. The pseudocolor decomposition result is shown as Fig. 5(d), in which the power of double bounce scattering, volume scattering and surface scattering are displayed by red, green, and blue, respectively.

The analysis of the slant ranges is shown in Fig. 6. The top of cube contributes to strong surface scattering, which appears leftmost in the image since the slant ranges of the EM waves incident on them are small. The scattering of ground is mainly composed of volume scattering since the ground is rough enough. The double bounce scattering contributes to a bright line on the right side of the surface scattering area. However, since the ground surface is rough, the slant ranges of all the double bounce scattering are not equal actually. Therefore, the

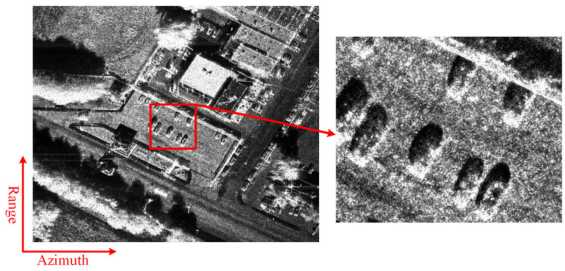

Fig. 7. MiniSAR images of Kirtland AFB.

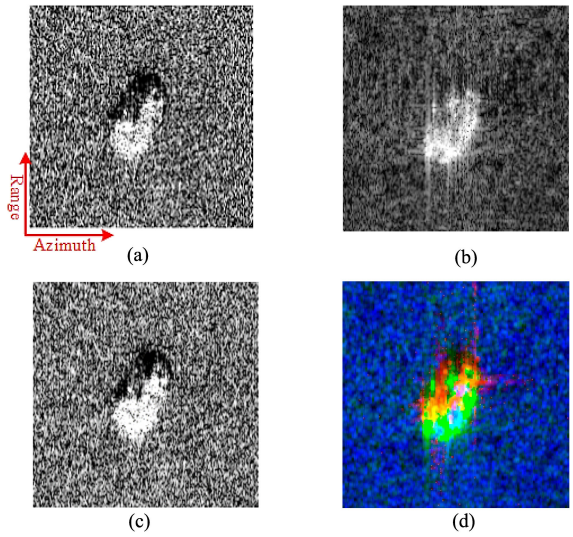

Fig. 8. Simulated polarimetric SAR images of a family car with freeman decomposition result.

double bounce scattering does not contribute to an ideal line, but a thick line. Meanwhile, the roughness of the ground surface also contributes to the defocusing phenomena. For example, there are some patches of pale red in the shadow area, which should not exist under ideal conditions.

C. Scattering Mechanism Validation of a Car

To further verify the correctness of the simulated images, a MiniSAR image of Kirtland AFB, shown in Fig. 7, is presented for comparison with the simulated images, which includes many family cars. The MiniSAR image is provided by the Sandia National Laboratories and is free to download [37].

A simulation scenario, shown in Fig. 2, is used to simulate polarimetric SAR images, which includes a random surface and a family car with an orientation angle of 30°. The radar parameters are given in Table I and the simulated polarimetric SAR images are shown in Fig. 8 with Freeman decomposition result.

The simulated HH channel SAR image in Fig. 8 is in good agreement with that of MiniSAR platform in Fig. 7. There appeared to be subtle differences in the structure, since there may be differences in the structural details between the target's CAD model and the actual vehicle. Typical effects of polarimetric SAR system, such as shadow, are clearly visible behind the car. The intensity of ground surface in cross-polarized images is

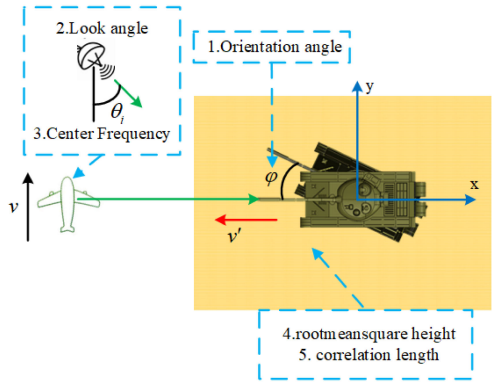

Fig. 9. Parameters that change in all experiments.

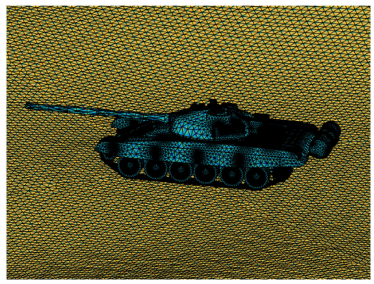

Fig. 10. Model of the simulation scenario in experiment E1.

weaker compared with the co-polarized images, which makes the shadow indiscernible. The Freeman decomposition result is also presented. Dihedral corner reflectors are formed between the car and the ground, which lead to strong double bounce scattering. The scattering of the target is quite complex and thus the volume scattering is particularly strong in the area of target. The simulated polarimetric SAR images of the cube and the family car validate the effectiveness of the proposed polarimetric observation simulation.

D. Influencing Factors Analysis of Scattering Mechanism

In this section, a T-72 main battle tank modeled based on the structure of real target, is used to simulate the PolSAR images. Its scattering mechanism is analyzed by data simulated under different observation conditions with the proposed method. The parameters of the PolSAR system are given in Table I, in which the center frequency, look angle and resolution are the variables of the simulation experiments. Fourteen sets of simulations are performed, whose detailed simulation parameters are given in Table III and the size of the random surface is 30 m × 30 m in all simulations. Five parameters are changed in all simulation experiments, which are shown in Fig. 9. The results are given as follow and Freeman decomposition is used to analyze the typical scattering mechanism of the whole scenario in different simulation cases.

In experiment E1, the correlation length and RMS height of the small-scale random surface are set as 4.6 and 2 cm whereas those of the large-scale random surface are 500 and 0.5 cm. The EM parameters of the surface are the same as those of dry soil. The model of the target and surface is shown in Fig. 10.

TABLE III
PARAMETERS OF EACH SIMULATION EXPERIMENT

Serial number	Small-scale random surface		Large-scale random surface		Look angle of radar θ_i (deg)	Orientation angle of target φ (deg)	Center frequency (GHz)	Resolution
	l_1 (cm)	δ_1 (cm)	l_2 (cm)	δ_2 (cm)				
E1	4.6	2	500	0.5	28	0	16.8GHz	$0.1m \times 0.1m$
E2						30		
E3						60		
E4						90		
E5						120		
E6						150		
E7						180		
E8					20	0		
E9					36			
E10					45			
E11					28		10GHz	$0.3m \times 0.3m$
E12							35GHz	$0.1m \times 0.1m$
E13	30	2					16.8GHz	
E14	4.6	0.2						

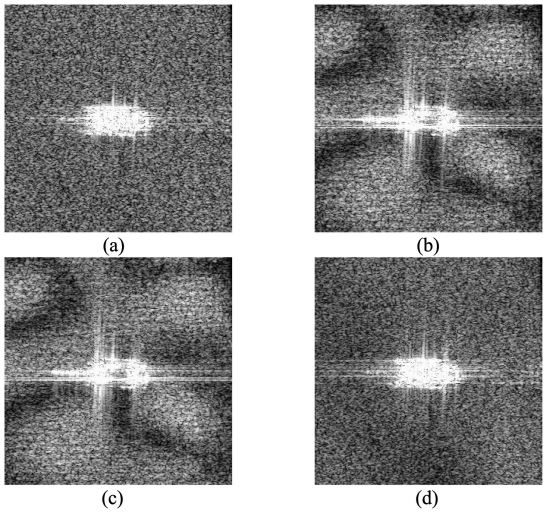

Fig. 11. Simulated PolSAR images of experiment E1.

TABLE IV
SCATTERING COMPONENT PERCENTAGE OF TARGET IN EXPERIMENT E1

Scattering components	Surface scattering	Double-bounce scattering	Volume scattering
Percentage (%)	11.48	40.62	47.90

The look angle of radar is 28° and the orientation angle of the target is 0°, which means the orientation of tank is perpendicular to the movement direction of radar.

The simulated PolSAR images of experiment E1 are shown in Fig. 11. Taken as a whole, the scattering of cross-polarized images is weaker than that of co-polarized images. However, the scattering of gun barrel region is obviously stronger in the cross-polarized images. Freeman decomposition is performed to investigate the scattering mechanism, whose result is shown in Fig. 12.

The target is segmented to calculate the proportion of the scattering components, and the results are given in Table IV. According to the decomposition results, the even-scattering ratio of the tank body is 40.62%, and the volume scattering is 47.90%. The volume scattering is particularly strong in the area of gun barrel, whereas the scattering from the tank's body is mainly a combination of double-bounce scattering and volume scattering. It shows strong surface scattering and weak volume scattering in the area of background surface, since the surface is relatively flat.

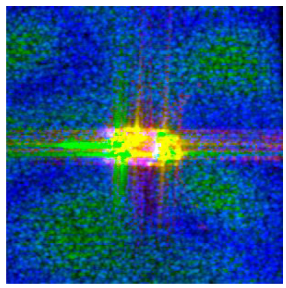

Fig. 12. Freeman decomposition result of PolSAR images in experiment E1.

Taking the results of experiment E1 as benchmarks, one can reveal the scattering mechanism by comparing following experimental results obtained by simulation under different conditions.

1) Influence of Orientation Angle: The scattering characteristics of the target may vary widely as the orientation angle of target changes. The impacts of orientation angle on the scattering mechanism of target are studied in experiments E2–E7, in which the orientation angles are set from 30° to 180° with an interval of 30°. The HH channel images of the simulated PolSAR images in experiments E2–E7 are shown in Fig. 13 and the Freeman decomposition results are shown in Fig. 14.

According to the scattering component percentage of target given in Table V, as the orientation angle increases, the proportions of volume scattering components and double bounce scattering components vary greatly. When the orientation angles are $0^\circ, 90^\circ$and 180°, the proportion of double bounce scattering components is relatively large, which is 40.62%, 43.56%, and 40.40%, respectively. This is because the dihedral corner reflectors in the turret and auxiliary fuel tank areas are perpendicular to the incident direction in these cases. On the contrary, there are more volume scattering components when orientation angles are $30^\circ, 60^\circ, 120^\circ$, and 150° because the ideal dihedral corner reflectors are difficult to form.

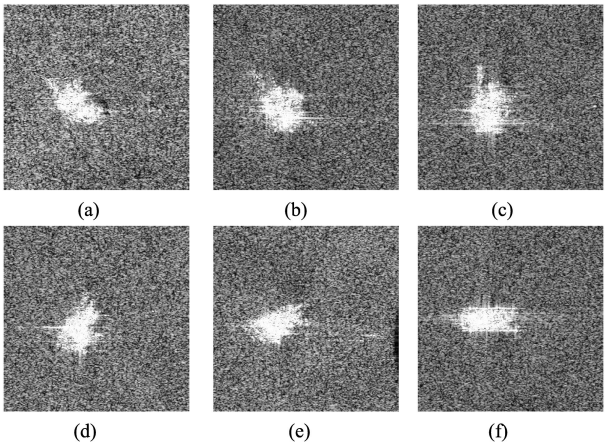

Fig. 13. HH channel images of the simulated PolSAR images in experiment E2–E7 (with different orientation angles).

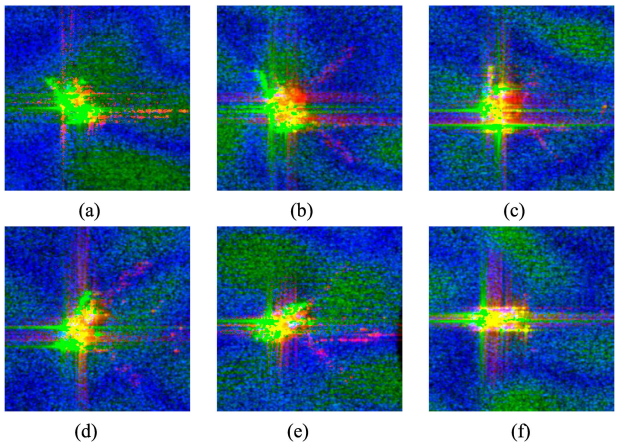

Fig. 14. Freeman decomposition results of experiments E2–E7.

TABLE V
SCATTERING COMPONENT PERCENTAGE OF TARGET IN EXPERIMENT E2–E7

Experiment serial number	Surface scattering (%)	Double-bounce scattering (%)	Volume scattering (%)
E2 (φ=30°)	1.91	22.84	75.25
E3 (φ=60°)	3.01	37.97	59.02
E4 (φ=90°)	7.90	43.56	48.54
E5 (φ=120°)	6.07	36.43	57.50
E6 (φ=150°)	7.99	36.23	55.78
E7 (φ=180°)	12.44	40.40	47.16

2) Influence of Look Angle: Experiments E8–E10 are intended to find out the impact of look angle on the scattering mechanism. The look angles are set as 20°, 36°, and 45° respectively whereas other parameters are the same as those in experiment E1. The simulated HH channel PolSAR images are shown in Fig. 15, whose Freeman decomposition results are shown in Fig. 16.

As the look angle increases, the projection of the target on the slant range becomes longer, so the range-direction length of the target in the image becomes larger. Besides, the various

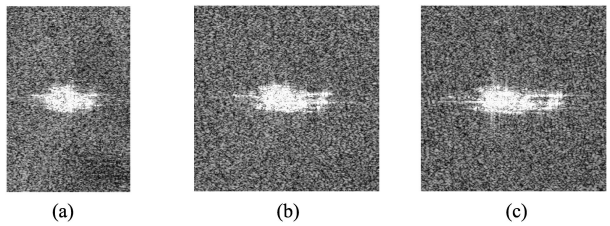

Fig. 15. HH channel images of experiment E8-E10 (with different look angles).

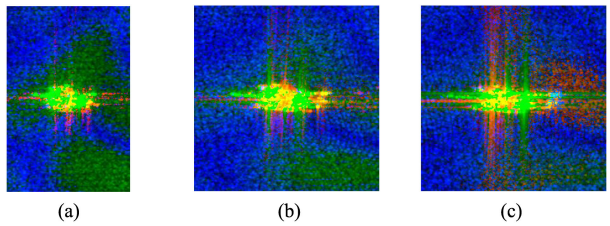

Fig. 16. Freeman decomposition results of experiments E8–E10.

TABLE VI
SCATTERING COMPONENT PERCENTAGE OF TARGET IN EXPERIMENT E8-E10

Experiment serial number	Surface scattering (%)	Double-bounce scattering (%)	Volume scattering (%)
E8 ($\theta_i = 20^\circ$)	1.39	27.98	70.63
E9 ($\theta_i = 36^\circ$)	3.08	36.71	60.20
E10 ($\theta_i = 45^\circ$)	1.62	32.00	66.38

parts of the tank appear more scattered on the image when the look angle is large. The image of the auxiliary fuel tanks is far away from that of the tank body, which contributes to the smearing effect at the rear part of the target. Furthermore, the scattering components of target are greatly different, which are given in Table VI. When the look angle is 20°, volume scattering is quite strong on the body of tank, accounting for 70.63%. As the look angle increases, volume scattering components decrease and the double bounce scattering components increase. Nevertheless, the double bounce scattering components of the target is strongest when the look angle is 28°. When the look angle increases to 36° and 45°, the percentage of the double bounce scattering components decreases to 36.71% and 32.00% again, and that of the volume scattering components increases to 60.20% and 66.38%.

To explained that, we might consider the effects of structure characters on the propagation of EM wave. When the look angle is small, the scattering of facets in one pixel is dense and thus volume scattering components are easier to generate. Dihedral corner reflector can be formed more easily as the look angle increases. As a result, double bounce scattering components become dominant on the body of the tank. When the look angle is larger, ideal dihedral corner reflectors reduce because more complex scattering occurs, thus volume scattering components increase.

3) Influence of System Center Frequency: The center frequency has an impact on the scattering mechanism as well.

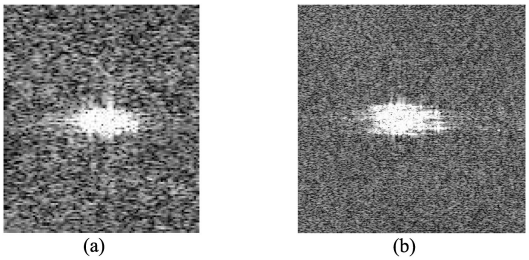

(a) (b)

Fig. 17. HH channel images of experiment E11 and E12 (the center frequency and resolution of E11 are 10 GHz and $0.3\ \mathrm{m} \times 0.3\ \mathrm{m}$, whereas those of E12 are 35 GHz and $0.1\ \mathrm{m} \times 0.1\ \mathrm{m}$).

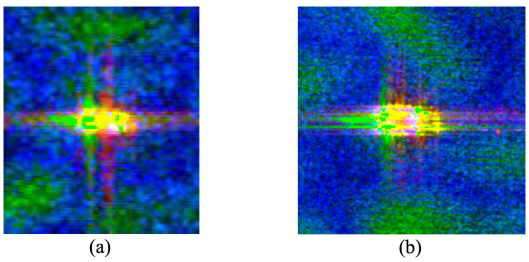

(a) (b)

Fig. 18. Freeman decomposition results of experiments E11 and E12.

TABLE VII
SCATTERING COMPONENT PERCENTAGE OF TARGET IN EXPERIMENT E11–E12

Experiment serial number	Surface scattering (%)	Double-bounce scattering (%)	Volume scattering (%)
E11	9.79	40.01	50.21
E12	13.08	39.60	47.32

In experiment E11, center frequency is set as 10 GHz and the resolution is $0.3\ \mathrm{m} \times 0.3\ \mathrm{m}$. The parameters of radar system are set up according to the moving and stationary target acquisition and recognition dataset, which is published by the Defense Advanced Research Projects Agency [38].

In experiment E12, the center frequency is changed into 35 GHz to investigate the variety of the scattering characteristics with the center frequency. The HH channel images are shown in Fig. 17 and the Freeman decomposition results are shown in Fig. 18.

When the center frequency and the resolution decrease, as shown in Figs. 17(a) and 18(a), the structure of the target is difficult to distinguish and the distribution of scattering components becomes simpler. In experiment E12, the Freeman decomposition provides more information of the structure compared to that of experiment E1, which shows clear texture of auxiliary fuel tanks at the rear part of the target. The shape of the auxiliary fuel tanks is visible, which makes it feasible to extract scattering properties contributed by tail devices. On the basis of the findings, it can be concluded that more texture information and structure details can be obtained when the center frequency is higher. However, according to the scattering component percentage given in Table VII, there is little difference in the proportion of scattering components between these experiments.

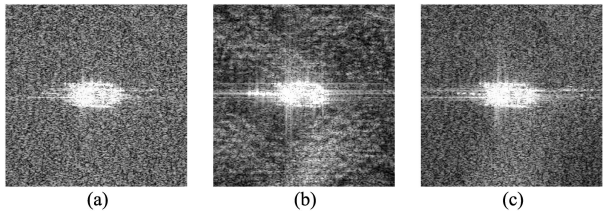

(a) (b) (c)

Fig. 19. Simulated PolSAR images of experiment E13 (larger correlation length of small-scale surface).

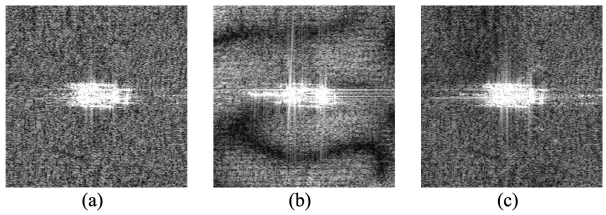

(a) (b) (c)

Fig. 20. Simulated PolSAR images of experiment E14 (smaller RMS height of small-scale surface).

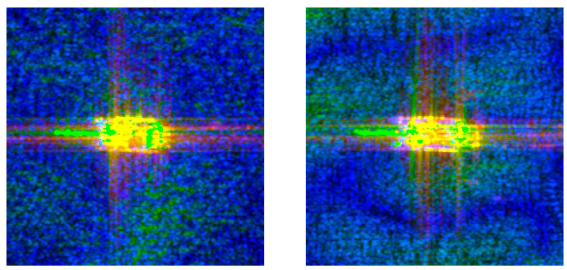

(a) (b)

Fig. 21. Freeman decomposition results of experiments E13 and E14.

TABLE VIII
SCATTERING COMPONENT PERCENTAGE OF TARGET IN EXPERIMENTS E13 AND E14

Experiment serial number	Surface scattering (%)	Double-bounce scattering (%)	Volume scattering (%)
E13	4.27	44.43	51.30
E14	8.28	43.59	48.14

4) Influence of Background Surface Roughness: Experiments E13 and E14 are performed to study the scattering mechanism of the target with background surface of different fluctuation conditions. Compared with experiment E1, the correlation length of the small-scale surface is larger in experiment E13 and thus the tiny fluctuation of the surface will become gentler. The RMS height of the small-scale surface is smaller in experiment E14 compared to that in experiment E1. The simulated PolSAR images of experiments E13 and E14 are shown in Figs. 19 and 20. Freeman decomposition results are shown in Fig. 21.

The scattering component percentage is given in Table VIII. In experiment E13, since the ground is more flat, the dihedral corner reflector is much easier to form between the target and the ground. Therefore, the proportion of the double bounce scattering of the target in experiment E13 increases to 44.43% compared with experiment E1. Besides, the texture of the HV channel in experiment E13 becomes more complicated, since

TABLE IX
CONFIGURATION AND PROGRAMMING MODEL OF THE SYSTEM

System	CPU	GPU
Hardware	Intel Core i9-9900K 3.6GHz	NVIDIA GeForce RTX 2080 Ti
Programming model	MS-MPI 10.0	CUDA 9.2

the fluctuation of the small-scale surface is sparser than that in experiment E1. The same scattering mechanism is observed in experiment E14. The small-scale surface in experiment E14 is gentler than that in experiment E1 and thus the volume scattering is weaker. The proportion of the double bounce scattering on the body of target increases to 43.59%, which show similar scattering mechanism with that in experiment E13.

E. Computational Efficiency

In this section, the simulation time and computational burden of some experiments are presented to analyze the calculation efficiency.

In our experiments, all the programs are written in C++ by Microsoft Visual Studio 2017. However, the recurrent high-complexity operations, such as FFTs and IFFTs, impose a huge computational burden. Therefore, CPU parallelization based on Microsoft Message Passing Interface (MS-MPI) [39] and GPU parallelization based on NVIDIA Compute Unified Device Architecture (CUDA) [40] are both used to improve the operation efficiency. MS-MPI is an implementation of parallel programming for CPU developed by Microsoft and CUDA is a framework for GPU parallelization presented by NVIDIA.

The computational efficiency of considered implementations is tested with a system, whose configuration and programming model are given in Table IX.

Take the scenario of experiment E1 in Section III-D for example, the computation burden and efficiency are discussed. The calculation time of each pulse in each polarization channel is about 1.63 s, which is acceptable. However, in order to acquire the simulated images according to the PolSAR imaging procedure, thousands of pulses with four polarization modes need to be calculated. Therefore, the execution time of the serial implementation is up to 46.92 h. By applying CPU+GPU collaborative computing, the execution time is reduced to 3.44 h with the memory footprint of 3.27 GB. In our future work, the computational efficiency will be further improved by calculating the scattered field of each facet in parallel.

IV. CONCLUSION

In this article, an efficient simulation framework of PolSAR images is presented to analyze the scattering mechanism of man-made target in PolSAR images under various conditions. Ray tracing based on GO/PO/KA hybrid method is used to perform the EM scattering calculation and generate the simulated PolSAR images. The method is validated by comparing the simulated image with the measured MiniSAR data. A simulation scenario including a T-72 tank and a double-scale random surface is built to investigate the scattering mechanism of the tank as well. Several simulation experiments are performed under various observation conditions, radar parameters and terrains. Based on the simulation results, scattering mechanism of the tank under different situations is analyzed by Freeman decomposition. Scattering component percentages of the target are also presented, from which the differences of the scattering properties under different conditions are analyzed both in qualitative and quantitative ways. Simulation and scattering mechanism analysis method can be used to analyze the polarimetric scattering mechanism of any actual target under various observation conditions in a quantitative way. Based on this, feature extraction methods for specific targets can be designed, which is valuable for the target detection and recognition.

REFERENCES

[1] J. Yin, W. M. Moon, and J. Yang, "Novel model-based method for identification of scattering mechanisms in polarimetric SAR data," *IEEE Trans. Geosci. Remote Sens.*, vol. 54, no. 1, pp. 520–532, Jan. 2016.
[2] M. Jafari, Y. Maghsoudi, and M. J. Valadan Zoej, "A new method for land cover characterization and classification of polarimetric SAR data using polarimetric signatures," *IEEE J. Sel. Topics Appl. Earth. Observ. Remote Sens.*, vol. 8, no. 7, pp. 3595–3607, Jul. 2015.
[3] R. Paladini, M. Martorella, and F. Berizzi, "Classification of man-made targets via invariant coherency-matrix eigenvector decomposition of polarimetric SAR/ISAR images," *IEEE Trans. Geosci. Remote Sens.*, vol. 49, no. 8, pp. 3022–3034, Aug. 2011.
[4] G. Yao, C. Ke, X. Zhou, H. Lee, X. Shen, and Y. Cai, "Identification of alpine glaciers in the Central Himalayas using fully polarimetric L-band SAR data," *IEEE Trans. Geosci. Remote Sens.*, vol. 58, no. 1, pp. 691–703, Jan. 2020.
[5] T. Zhang, J. Ji, X. Li, W. Yu, and H. Xiong, "Ship detection from PolSAR imagery using the complete polarimetric covariance difference matrix," *IEEE Trans. Geosci. Remote Sens.*, vol. 57, no. 5, pp. 2824–2839, May 2019.
[6] Y. Liu, W. Wang, S. Dai, B. Rao, and G. Wang, "A unified multimode SAR raw signal simulation method based on acquisition mode mutation," *IEEE Geosci. Remote Sens. Lett.*, vol. 14, no. 8, pp. 1233–1237, Aug. 2017.
[7] S. Cimmino, G. Franceschetti, A. Iodice, D. Riccio, and G. Ruello, "Efficient spotlight SAR raw signal simulation of extended scenes," *IEEE Trans. Geosci. Remote Sens.*, vol. 41, no. 10, pp. 2329–2337, Oct. 2003.
[8] T. Balz and U. Stilla, "Hybrid GPU-based single- and double-bounce SAR simulation," *IEEE Trans. Geosci. Remote Sens.*, vol. 47, no. 10, pp. 3519–3529, Oct. 2009.
[9] G. Chen, S. Yang, and D. Su, "An accurate three-dimensional FDTD(2,4) method on face-centered cubic grids with low numerical dispersion," *IEEE Antennas Wireless Propag. Lett.*, vol. 18, no. 9, pp. 1711–1715, Sep. 2019.
[10] A. Taflove and S. C. Hagness, "Electrodynamics entering the 21st century," in *Computational Electrodynamics: The Finite-Difference Time-Domain Method*, 3rd ed., Norwell, MA, USA: Artech House, 2005, pp. 3–10.
[11] S. Liu, B. Zou, L. Zhang, and S. Ren, "Heterogeneous CPU+GPU-accelerated FDTD for scattering problems with dynamic load balancing," *IEEE Trans. Antennas Propag.*, vol. 68, no. 9, pp. 6734–6742, Sep. 2020.
[12] S. Liu, B. Zou, L. Zhang, and S. Ren, "A multi-GPU accelerated parallel domain decomposition one-step leapfrog ADI-FDTD," *IEEE Antennas Wireless Propag. Lett.*, vol. 19, no. 5, pp. 816–820, May 2020.
[13] M. S. Ferdous, U. H. Himi, P. McGuire, D. T. Power, T. Johnson, and M. J. Collins, "C-band simulations of melting icebergs using GRECOSAR and an EM model: Varying wind conditions at lower beam mode," *IEEE J. Sel. Topics Appl. Earth. Observ. Remote Sens.*, vol. 12, no. 12, pp. 5134–5146, Dec. 2019.
[14] G. Di Martino, A. Iodice, D. Poreh, and D. Riccio, "Pol-SARAS: A fully polarimetric SAR raw signal simulator for extended soil surfaces," *IEEE Trans. Geosci. Remote Sens.*, vol. 56, no. 4, pp. 2233–2247, Apr. 2018.
[15] G. Guo, L. Guo, and R. Wang, "ISAR image algorithm using time-domain scattering echo simulated by TDPO method," *IEEE Antennas Wireless Propag. Lett.*, vol. 19, no. 8, pp. 1331–1335, Aug. 2020.
[16] I. Gershenzon, Y. Brick, and A. Boag, "Shadow radiation iterative physical optics method for high-frequency scattering," *IEEE Trans. Antennas Propag.*, vol. 66, no. 2, pp. 871–883, Feb. 2018.

[17] M. Zhang, Y. Zhao, J. Li, and P. Wei, "Reliable approach for composite scattering calculation from ship over a sea surface based on FBAM and GO-PO models," *IEEE Trans. Antennas Propag.*, vol. 65, no. 2, pp. 775–784, Feb. 2017.

[18] J. Li, M. Zhang, L. Wang, and Y. Jiao, "An efficient way for studying the EM scattering from a marine environment with multiple ships," *IEEE Antennas Wireless Propag. Lett.*, vol. 19, no. 9, pp. 1526–1530, Sep. 2020.

[19] H. Ling, R. Chou, and S. Lee, "Shooting and bouncing rays: Calculating the RCS of an arbitrarily shaped cavity," *IEEE Trans. Antennas Propag.*, vol. 37, no. 2, pp. 194–205, Feb. 1989.

[20] Y. Tao, H. Lin, and H. Bao, "GPU-based shooting and bouncing ray method for fast RCS prediction," *IEEE Trans. Antennas Propag.*, vol. 58, no. 2, pp. 494–502, Feb. 2010.

[21] J. Huo, L. Xu, X. Shi, and Z. Yang, "An accelerated shooting and bouncing ray method based on GPU and virtual ray tube for fast RCS prediction," *IEEE Antennas Wirel. Propag. Lett.*, vol. 20, no. 9, pp. 1839–1843, Sep. 2021.

[22] C. Dong, L. Guo, and X. Meng, "An accelerated algorithm based on GO-PO/PTD and CWMFSM for EM scattering from the ship over a sea surface and SAR image formation," *IEEE Trans. Antennas Propag.*, vol. 68, no. 5, pp. 3934–3944, May 2020.

[23] G. Guo and L. Guo, "SBR method for near-field scattering of an electrically large complex target illuminated by dipole sources," *IEEE Access*, vol. 6, pp. 78710–78718, 2018.

[24] Y. Zhao, M. Zhang, Y. Zhao, and X. Geng, "A bistatic SAR image intensity model for the composite ship-ocean scene," *IEEE Trans. Geosci. Remote Sens.*, vol. 53, no. 8, pp. 4250–4258, Aug. 2015.

[25] P. Liu and Y. Jin, "A study of ship rotation effects on SAR image," *IEEE Trans. Geosci. Remote Sens.*, vol. 55, no. 6, pp. 3132–3144, Jun. 2017.

[26] G. Margarit, J. J. Mallorqui, J. M. Rius, and J. Sanz-Marcos, "On the usage of GRECOSAR, an orbital polarimetric SAR simulator of complex targets, to vessel classification studies," *IEEE Trans. Geosci. Remote Sens.*, vol. 44, no. 12, pp. 3517–3526, Dec. 2006.

[27] G. Margarit, J. J. Mallorqui, J. Fortuny-Guasch, and C. Lopez-Martinez, "Phenomenological vessel scattering study based on simulated inverse SAR imagery," *IEEE Trans. Geosci. Remote Sens.*, vol. 47, no. 4, pp. 1212–1223, Apr. 2009.

[28] Y. Jin and F. Xu, "Basic of polarimetric scattering," in *Polarimetric Scattering and SAR Information Retrieval*. Singapore: Wiley, 2013, pp. 16–19.

[29] R. Wang, G. Guo, Z. He, and L. Guo, "Scattering prediction of target above layered rough surface based on time-domain ray tracing modeling," *IEEE Trans. Antennas Propag.*, vol. 69, no. 5, pp. 2820–2832, May 2020.

[30] F. Giorgio and D. Riccio, "Analytic formulations of electromagnetic scattering," in *Scattering, Natural Surfaces, and Fractals*. Burlington, MA, USA: Elsevier, 2006, pp. 118–134.

[31] W. Gordon, "Far-field approximations to the kirchoff-Helmholtz representations of scattered fields," *IEEE Trans. Antennas Propag.*, vol. 23, no. 4, pp. 590–592, Jul. 1975.

[32] "Dielectric constants of common materials," 2018. [Online]. Available: https://www.kabusa.com/Dilectric-Constants.pdf

[33] S. Ridha, S. Irawan, and B. Ariwahjoedi, "Prediction of interface conductivity of cement slurry during early hydration considering the effect of curing temperature and pressure," in *Proc. IEEE Symp. Ind. Electron. Appl.*, 2011, pp. 114–119.

[34] E. Knott, T. Senior, and P. Uslenghi, "High-frequency backscattering from a metallic disc," *Proc. Inst. Elect. Eng.*, vol. 118, no. 12, pp. 1736–1742, Dec. 2010.

[35] J. Lee and E. Pottier, "Polarimetric SAR speckle statistics," in *Polarimetric Radar Imaging: From Basics to Applications*, 1st ed., Boca Raton, FL, USA: CRC Press, 2009, pp. 101–102.

[36] A. Freeman and S. L. Durden, "A three-component scattering model for polarimetric SAR data," *IEEE Trans. Geosci. Remote Sens.*, vol. 36, no. 3, pp. 963–973, May 1998.

[37] D. Gutierrez, "miniSAR: A review of 4-inch and 1-foot resolution ku-band imagery," Jun.–Feb., 2005. [Online]. Available: https://www.sandia.gov/radar/complex-data/index.html

[38] "The air force moving and stationary target recognition database," 2014. [Online]. Available: https://www.sdms.afrl.af.mil/index.php?collection=mstar

[39] "Microsoft MS-MPI v10.0," 2018. [Online]. Available: https://docs.microsoft.com/en-us/message-passing-interface/microsoft-mpi-release-notes

[40] J. Cheng, *Professional CUDA C Programming*. Birmingham, U.K.: Wrox Press, 2014.

Lamei Zhang (Senior Member, IEEE) received the B.S., M.Sc., and Ph.D. degrees in information and communication engineering from the Harbin Institute of Technology, Harbin, China, in 2004, 2006 and 2010, respectively.

She is currently an Associate Professor with the Department of Information Engineering, Harbin Institute of Technology. She is currently the Secretary of the IEEE Harbin Geoscience and Remote Sensing Chapter. Her research interests include remote sensing images processing, information extraction, and intelligent interpretation of high-resolution SAR, polarimetric SAR, and polarimetric SAR interferometry.

Yifan Chen was born in Wuxi, China in 1996. He received the B.S. degree with the School of Physics and Engineering, Zhengzhou University, Zhengzhou, China, in 2018. He is currently working toward the Ph.D. degree with the Department of Information Engineering, Harbin Institute of Technology, Harbin, China.

His research interests include scattering properties and characteristics of radar targets.

Ning Wang received the B.S. and M.Sc. degrees in mathematics, and the Ph.D. degrees in computer science and technology from Harbin Institute of Technology, Harbin, China, in 2006, 2008 and 2013.

He is currently a Senior Engineer of radar electrical system with Beijing Institute of Radio Measurement, Beijing, China. His current research interests include space target radar signal processing, recognition, ISAR imaging, three-dimensional reconstruction, and pose estimation.

Bin Zou (Senior Member, IEEE) received the B.S. degree in electronic engineering and the Ph.D. degree in information and communication engineering from Harbin Institute of Technology, Harbin, China, in 1990, and 2001, respectively, and the M.Sc. degree in space studies from the International Space University, Strasbourg, France, in 1998.

He is currently a Professor with the Department of Information Engineering, Harbin Institute of Technology. He is currently the Chair of IEEE HARBIN GEOSCIENCE AND REMOTE SENSING chapter. His research interests include SAR image processing, polarimetric SAR, and polarimetric SAR interferometry.

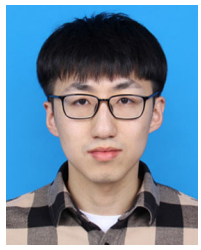

Shuo Liu (Student Member, IEEE) was born in Harbin, China, in 1993. He received the B.Sc. and M.Sc. degrees from the Harbin Institute of Technology, Harbin, China, in 2016 and 2018, respectively. He is currently working toward the Ph.D. degree in information and communication engineering with the Department of Information Engineering.

He is currently working on the high-performance electromagnetic simulation and its application to remote sensing.